Correlative study of structural and optical properties of ZnSe under severe plastic deformation

B. Sotillo[1*], G. Escalante[1,2], C. Radoi[1], V. Muñoz-Sanjosé[3], J. Piqueras[1], P. Fernández[1]

[1]Department of Materials Physics, Faculty of Physics, Complutense University of Madrid, 28040, Madrid, Spain.

[2] Tepeaca Higher Technological Institute. National Technological of Mexico, 75200, Tepeaca, Mexico

[3] Department of Applied Physics and Electromagnetism, University of Valencia, Valencia, 46010 Spain

* Corresponding author: bsotillo@ucm.es

Abstract. The effect of plastic deformation on the optical and structural properties of ZnSe crystals has been investigated. The optical properties have been monitored by cathodoluminescence measurements as a function of the deformation degree. Remarkable differences in the defect related emissions from the most severely deformed areas have been encountered. Deformation of the crystal lattice of ZnSe, associated to slip phenomena, has been studied by means of Electron Backscattered Diffraction (EBSD) and micro-Raman spectroscopy. The relation between the deformation and the optical properties of the ZnSe crystals has been described.

1. Introduction

Zinc Selenide (ZnSe) is a semiconductor material of the II-VI group. It has a direct bandgap in the blue range (2.7 eV) and zinc-blende crystal structure. The direct bandgap, responsible for the intense luminescence emissions, and the chemical stability, characteristic of most of the II-VI, are related to some of the most relevant optoelectronic applications. In the case of ZnSe, its use has been proposed for the development of blue light emitting diodes and laser diodes [1-3]. In addition to thin films and macroscopic crystals, ZnSe has been obtained in a great variety of morphologies in the nanometric range, that make it suitable for applications such as field emitters, sensors, actuators, LEDs, and many other optoelectronic devices [4]. ZnSe is also widely used in IR optical applications as it offers low absorption in the IR spectral region [5,6]. For many of its applications, mechanical stability of the material is always desirable. In the case of the applications of ZnSe bulk crystals, a good crystalline quality along with the understanding of the defects that can influence the luminescence emission is important.

In this work, the effect of severe plastic deformation on the optical and structural properties of Solid Phase Recrystallization (SPR) crystals of ZnSe has been investigated by the application of Vickers indentations with variable load. In addition to previous cathodoluminescence and photoluminescence studies[7], we have combined luminescence measurements with micro-Raman spectroscopy and Electron Backscattered Diffraction (EBSD) to gain a deeper understanding of the modifications induced by severe plastic deformation. A detailed correlation between EBSD, CL and Raman mapping has been, to our knowledge, never reported.

2. Experimental

ZnSe samples are obtained from CVD-grown microcrystalline boules, and from boules after solid-phase recrystallization in Ar or Se atmospheres to obtain single crystals. Further information about the samples and their fabrication can be found in [7]. Briefly, it was an isothermal growth at 1000ºC during 17 days, introducing an overpressure of Ar or Se. The studied face of the sample was mechanically and mechano-chemically polished, as described in [7]. Vickers indentations were performed by a Zwick/Roell Indentec machine (ZHVμ), applying loads from 1 kp to 0.01 kp during 15 s. The accuracy of the loads applied fulfills the requirements of the ISO 6507 and ASTM E 384 standards. The morphology of the obtained indentation has been observed with an optical microscope attached to the indentation machine, as well as with a FEI Inspect SEM.

Cathodoluminescence (CL) measurements were done in a Hitachi S2500 SEM. For collecting the CL emission, a HAMAMATSU PMA-11 CCD with measurement range between 300 and 800 nm, coupled to an optical fibre, has been used. The wavelength resolution of the CCD is below 3 nm. All the measurements were carried out at room temperature. The characterization of crystal structure and orientation of the sample has been performed by Electron Backscatter Diffraction (EBSD) in a FEI Inspect SEM, working at 20 kV. The EBSD detector was a Bruker *e*⁻Flash. The analysis of the EBSD data has been performed with ESPRIT QUANTAX CrystAlign commercial software, and the patterns have been indexed to the ZnSe stilleite phase (F-43m). Micro-Raman and photoluminescence (PL) measurements were carried out in a confocal microscope Horiba JobinYvon LABRAM-HR. The Raman spectra were recorded under excitation with the 633 nm line of a He-Ne laser. The laser was focused onto the sample using a 100× Olympus objective (0.9 NA), and the scattered light was also collected using the same objective (backscattering configuration). The grating used to analyse the signal was of 1800 l/mm, and the signal was collected with an air-cooled CCD camera. The PL measurements were performed under excitation with 325 nm light from a He-Cd laser. The setup is the same as for the Raman measurements, just changing the objective (a Thorlabs LMU-40×-NUV objective (0.5 NA)) and the grating (600 l/mm). Raman and PL data were collected and analysed using the Labspec 5.0 software of the confocal microscope.

3. Results and discussion

A study of the effect of plastic deformation induced by an applied stress [8-10] and around a Berkovich nanoindentation [11] has been already performed. In this work, Vickers indentations have been produced on ZnSe samples recrystallized in Se and in Ar, respectively. The applied loads varied from 1 kp to 0.01 kp (from 9.807 N to 0.098 N). For loads above 0.2 kp, large cracks appear around the indentation. In table 1 the sizes of the indentations (d1 and d2 are the dimensions of the diagonals) for loads between 0.2 kp and 0.01 kp are shown, along with the corresponding value calculated for the Vickers hardness (HV). The hardness values are close to those reported in the literature [12-14].

Load (kp)	**d1 (μm)**	**d2 (μm)**	**HV**	**d1 (μm)**	**d2 (μm)**	**HV**
	Recrystallized Se			Recrystallized Ar		
0.2	59.0	62.5	100	66.8	68.8	81
0.1	41.6	43.2	103	47.1	47.8	83

0.05	28.0	29.4	112	33.1	34.0	83
0.025	20.6	21.1	107	23.7	24.9	79
0.01	12.0	12.9	120	15	15.8	78

Table 1. Size (d1 and d2 are the dimensions of the diagonals) and calculated HV values for various Vickers indentations on the ZnSe samples.

In order to investigate the nature of the different defects produced around the indentation, luminescence measurements have been performed. The spectra of the undeformed crystals is described in detail in [7]. The CL emission recorded around the indentations on the recrystallized sample has been compared with the emission from the CVD-as-grown sample. CL measurements have been recorded in three different points inside and outside the indentation (see insets of Fig. 1). CL spectra of the as-grown sample are shown in Fig. 1(a). The spectrum corresponding to a position outside the indentation (point 1) consists mainly of the emission 2.77 eV associated with the near-band edge; while the spectra recorded in points 2 and 3 (inside the indentation) showed a broad emission band with peaks at 2.6 and 2.77 eV. The emission peak at 2.6 eV is attributed to dislocations that are introduced during the indentation process [15], and some authors reported this band is due to inelastic scattering of free excitons at some unidentified centre [16]. Fig. 1(b) shows CL spectra of the sample recrystallized in Se atmosphere. All these spectra show emissions associated with near-band edge and dislocations, as the spectra of the as-grown sample, as well as a broad emission in the range of 1.9 - 2.4 eV, which is related to complexes of zinc vacancies (V_{Zn}) impurity and centers associated with the presence of Cu [7,17]. Even though the luminescence emission is different in both samples, the main difference is the decrease of the emission of 2.77 eV in the region of the indentation with respect to the undeformed region, as a consequence of the induced crystal damage. Although this effect is present in both samples, it is more visible in the recrystallized one. On the other hand, the emission of the defects band shows a relative an increase in the region close to the indentation center due to a higher concentration of native defects and dislocations inside the indentation[18].

As expected, the atmosphere in which the recrystallization takes place, plays an important role on the defect structure. This is clearly revealed through the comparison of the CL spectra discussed above with those obtained from samples recrystallized in an Ar atmosphere. CL spectra of the recrystallized sample in Ar represented in Fig. 2 show changes in the luminescence properties with respect to the sample treated in Se atmosphere. The spectrum recorded in the non-indented region (point 1) shows a broad band with resolved emission peaks at 2.6 and 2.77 eV, as well as the appearance of a shoulder at about 2.3 eV associated to complex $V_{Zn–Cu}$ [7,19]. However, in the region inside the indentation (points 2 and 3) only the emission at 2.6 eV is observed, which is related with the recombination of excitons at the dislocations [9,15]. From the luminescence measurements, it is clear that for all the samples, the region below the indentation tip (points 2, 3) is where the highest density of point defects and impurity radiative centers is induced along with the dislocations, whereas outside and but close to the indentation (point 1) the main effect is due to formation and slip of the dislocations.

Photoluminescence (PL) measurements have been recorded at different positions of an indentation (Fig. 3). In the PL map (Fig 3(a)) it is plotted the intensity ratio of a broad band centered at 2.1 eV band respect to the 2.7 eV band. Far away from the indentation, the PL spectrum of the pristine material (non-indented) is characterized by a narrow emission band centered at 2.7 eV (Fig 3(b)), which, as in the case of CL measurements, can be associated with

the near-band edge emission of ZnSe. As the point for recording the spectrum is closer to the indentation, the emission at 2.7 eV decreases and a defect-related emission (broad band centered at 2.1 eV) increases. The defect emission is clearly dominant in the region of the indentation. Close to the indentation, but outside it, less defect-related emission is detected, in comparison with the indent site (Fig. 3(b)). However, in this region a series of bright and dark lines are visible (Fig. 3(a)), whose origin has been related to the presence of slip bands [8], extending away from the indentation [11] or non-radiative centers associated to them. The PL intensity ratio variation is presented in the inset of Fig. 3(b), and the points (1, 2, 3, 4) where the spectra have been recorded are shown. Further information about the luminescence properties of ZnSe samples recrystallized in Ar and in Se atmosphere can be found in[7].

As observed from the differences in the CL emission for the samples recrystallized in different atmospheres, the defect structure is strongly influenced by the atmosphere. This has been already reported by Urbieta et al. [7] and attributed to the differences in the stoichiometry associated to the presence of native defects. However, the crystal lattice modification produced by the deformation are similar for both samples. The results presented from here are obtained from the samples recrystallized in Se atmosphere, due to the higher hardness value observed for it (see Table 1). In order to know the crystal orientation of the ZnSe samples, EBSD measurements have been performed. We define the XYZ axis following the orientation of the three edges of the sample, as displayed in Fig. 4(a). The typical recorded Kikuchi pattern is shown if Fig. 4(b), along with the simulation of the crystallographic planes identified using the Bruker software. This software uses the Hough transformation to identify the lines observed in the Kikuchi pattern that, by comparison with the data of ZnSe, allows the orientation of the cubic cell with respect of the XYZ axis of the sample, as shown in Fig. 4(c). The software is also able to collect the orientation of several points on the sample and plot all the information together in an inverse pole figure (IPF) (Fig. 4(e)). As can be extracted from these IPFs, the sample is mostly single crystal with the direction family <221> close to the three XYZ axis (Fig. 4(e), poles with stronger intensity, marked with a '*M*'). In some regions grain boundaries and twins are observed as described in [7]. The change in the orientation is shown in Fig. 4(d)-(e), and respect to the XYZ system the <210> direction is close to the Y axis (Fig. 4(e), points marked with a '*T*' in the pole figure). The region of the sample selected to do the indentations has the orientation shown in Fig. 4(c).

According with the EBSD crystallographic analysis, Vickers indentations are performed along a direction close to the [221].For the cubic structure of ZnSe, the main slip systems are $\{111\} < 110 >$ [14,20]. However, if the load is applied along [221] direction, the slip systems shown in table 2 could be activated,(where the values for the Schmid factor [20] are shown). The Schmid factor relates the load applied, F, with the resolved shear stress τ on the slip plane in the slip direction:

$$\tau = \frac{F}{A}\ cos\varphi \times cos\lambda$$

φ is the angle between the loading direction and the normal to the slip planes and λ is the angle between the loading direction and the slip direction. When the Schmid factor is different from zero, a shear stress induced by the applied load could be high enough to activate several slip systems. The higher the Schmid factor, the easier the slip. In our case, the systems $(\bar{1}\bar{1}1)[0\bar{1}\bar{1}]$ and $(\bar{1}\bar{1}1)[\bar{1}0\bar{1}]$ would be the preferential ones.

Slip plane	Slip direction	Schmid factor for [221] loading direction

(111)	$[01\bar{1}]$	0.23
	$[10\bar{1}]$	0.23
	$[\bar{1}10]$	0
$(\bar{1}\mathbf{11})$	$[\bar{1}0\bar{1}]$	0.14
	$[01\bar{1}]$	0.045
	[110]	0.18
$(1\bar{1}\mathbf{1})$	$[0\bar{1}\bar{1}]$	0.14
	$[10\bar{1}]$	0.045
	[110]	0.18
$(\bar{1}\bar{1}\mathbf{1})$	$[\bar{1}0\bar{1}]$	0.41
	$[0\bar{1}\bar{1}]$	0.41
	$[\bar{1}10]$	0

Table 2. Schmid factor for loading direction [221], considering the 12 possible independent slip systems

EBSD measurements allows to visualize the plastic deformation induced around the indentation. Fig. 5(a) shows the schematic of the orientation of the diagonals of the indentation with respect to the axis of the sample that were defined in Fig. 4. To image the effect of plastic deformation we resort to the inverse pole figures and their spatial maps [21] for the three directions of the sample (IPFX, IPFY and IPFZ) shown in in Fig. 5(b). The dark central region (black pixels) corresponds to the position of the indentation. The colour scale of these images indicates how close are the X, Y and Z direction of the sample to the main crystallographic directions <001>, <10$\bar{1}$> and <111>, as shown in the color codes of Fig. 5(c). Comparison of the colour scale of the points that are far from the indentation with those close to the indentation shows that there is a misorientation or lattice rotation (the crystal direction oriented along the X, Y or Z axis change), due to the indentation. For example, X direction rotates from [221] towards [101] (green) and towards [111] (dark blue) directions. This slight lattice rotation is also seen in the inverse pole figures (IPF) of Fig. 5(b), mainly in the X and Y direction, where a spread of points along an arc indicates the misorientation. This misorientation is higher closer to the indentation, where a change in the colour scale is more evident (see black arrow in Fig. 5(b)).

In order to gain more information about the stress around the indentation, Raman spectroscopy has been used. Raman measurements are commonly employed to study stress in semiconductor materials [22-24]. ZnSe has a zinc-blende crystal structure, belonging to the F-43m space group and T_d^2 point group. Due to this symmetry, it has three optical phonon modes T_{2g}. As it is partially ionic, the longitudinal optical mode (LO) and the transverse optical modes (TO) are split, the LO modes corresponding to higher wavenumber.

By considering a backscattering configuration, and that the incident and scattered light are oriented along the <221> direction, both phonons, LO and TO, would be detected for all possible

combinations of incident and scattered polarization. Fig. 6(a) shows a typical Raman spectrum of a non-indented ZnSe sample. The LO mode is centred at 252.4 cm^{-1}, and the TO mode at 205.5 cm^{-1}. The widths of these two peaks are 6.0 and 4.8 cm^{-1}, respectively (as obtained from the fitting of the peaks to a Gauss-Lorentz type curve). Around 140 cm^{-1} are located the peaks associated with the second order of the TA phonons (2TA, as TA modes are symmetry forbidden [25]). These three modes are also observed in the spectra recorded inside the indentation (Fig. 6(b)), and no new modes are visible, which rules out the existence of a phase transition as reported in other studies for high-load indentations [26].

The presence of stress is detected by the shift of the Raman peaks[27]. Typically, compressive stress will produce a shift of the Raman peak towards higher wavenumber, whereas tensile stress produces the opposite shift. Both LO and TO modes show shifts in the region of the indentation, in comparison with the position of these peaks in the undamaged material. Although the behaviour of both modes with the sign of the stress is the same, the TO is more sensitive to the same level of stress [24]. Considering also the smaller width of this peak, we have chosen the TO mode to plot the shift map around the indentation (Fig. 7). In Fig. 7(a) the SEM image of the studied indentation is shown as a guidance. All the Raman peaks show a decrease in intensity in the indentation (similar to the intensity of the TO mode shown in Fig. 7(b)), mostly along the diagonal lines, associated with damage and deformation induced in the crystal lattice. This is also observed in the map of the TO peak width (Fig. 7(c)), where an increase in the width is observed inside the indentation due to a decrease in the crystal quality. More interesting is the map of the TO shift in Fig. 7(d). Inside the indentation a shift of the peak towards higher wavenumber indicates compressive stress, due to the pressure applied by the indentation tip. At the edges of the indentation, narrow lines of tensile stress appear. Finally, patterns of tensile/compressive stress variation are visible, which can be associated with activation of slip systems of dislocations induced by the plastic deformation, as described for example in other semiconductor materials [28-30], but in our case a geometrical interpretation is not easy as at least two slip systems have been activated (see table 2). A similar behaviour has been observed in ZnTe deformed under a load gradient [31].

The stress produced by the indentation on the ZnSe crystal induces birefringence through the photoelastic effect[32]. In Fig.8a, an optical image of the indentations produced with 0.2 kp, 0.1 kp, 0.05 kp and 0.025 kp loads is shown. The presence of induced stresses is clearly visible when the sample is placed between crossed linear polarizers in an optical microscope. ZnSe has a cubic structure, so no birefringence is expected in the undamaged crystal. However, as shown in the optical image of the indentations obtained with the crossed polarizers (Fig. 8(b)), a stress-induced birefringence around the indentation track is observed. The region showing birefringence is larger for higher applied loads.

3. Conclusions

Luminescent and crystal lattice deformation produced by Vickers indentations on ZnSe samples recrystallized in Se or Ar atmospheres have been studied. It has been shown that the atmosphere used to recrystallize the ZnSe samples influences the hardness of the samples as well as the luminescent emission. Higher hardness values have been obtained for the Se-recrystallized sample. Regarding the luminescence, the highest density of radiative centers associated to dislocations has been formed at the tip of the indentation, where the deformation is expected to be more severe. The deformation around the indentation has been further studied with EBSD and Raman spectroscopy, relating these measurements to the activated slip systems and the local lattice rotation induced by the indentation. EBSD and Raman measurements also ruled out the

formation of other crystal phases in the indentation. Finally, it has been shown that the deformation and lattice rotation induce birefringence around the different indentations.

Acknowledgements

Authors are grateful to the Spanish Ministry of Science, Innovation and Universities for support via the project MINECO/FEDER-MAT2015-65274-R. B. Sotillo acknowledges financial support from Comunidad de Madrid (Ayudas del Programa de Atracción de Talento).

References

1 H. Ishikura, T. Abe, N. Fukuda, H. Kasada, and K. Ando, Applied Physics Letters **76,** 1069 (2000).
2 H. Luo and J. Furdyna, Semiconductor science and technology **10,** 1041 (1995).
3 M. Haase, J. Qiu, J. DePuydt, and H. Cheng, Applied Physics Letters **59,** 1272 (1991).
4 J. Jie, W. Zhang, I. Bello, C.-S. Lee, and S.-T. Lee, Nano today **5,** 313 (2010).
5 D. C. Harris, Infrared physics & technology **39,** 185 (1998).
6 E. Gavrushchuk, Inorganic Materials **39,** 883 (2003).
7 A. Urbieta, P. Fernández, J. Piqueras, and V. Munoz, Materials Science and Engineering: B **78,** 105 (2000).
8 P. Fernández, J. Piqueras, A. Urbieta, Y. Rebane, and Y. Shreter, Semiconductor science and technology **14,** 430 (1999).
9 Y. Shreter, Y. Rebane, O. Klyavin, P. Aplin, C. Axon, W. Young, and J. Steeds, Journal of crystal growth **159,** 883 (1996).
10 P. Fernández, J. Piqueras, A. Urbieta, Y. T. Rebane, and Y. Shreter, Solid State Phenomena **63-64,** 207 (1998).
11 W.-H. Yau, P.-C. Tseng, H.-C. Wen, C.-H. Tsai, and W.-C. Chou, Microelectronics Reliability **51,** 931 (2011).
12 I. Yonenaga, Physica B: Condensed Matter **308,** 1150 (2001).
13 S. Grillo, M. Ducarroir, M. Nadal, E. Tournie, and J. Faurie, Journal of Physics D: Applied Physics **36,** L5 (2002).
14 I. Yonenaga and T. Suzuki, Philosophical magazine letters **82,** 535 (2002).
15 S. Myhajlenko, J. Batstone, H. Hutchinson, and J. Steeds, Journal of Physics C: Solid State Physics **17,** 6477 (1984).
16 P. Dean, P. Wright, and B. Cockayne, Journal of Physics C: Solid State Physics **16,** 3493 (1983).
17 A. Thomas, G. Russell, and J. Woods, Journal of Physics C: Solid State Physics **17,** 6219 (1984).
18 J. Mass, M. Avella, J. Jiménez, M. Callahan, D. Bliss, and B. Wang, Journal of Materials Research **22,** 3526 (2007).
19 J. A. Garcia, A. Remon, A. Zubiaga, V. Muñoz-Sanjosé, and C. Martinez-Tomás, physica status solidi (a) **194,** 338 (2002).
20 D. Hull and D. J. Bacon, *Introduction to dislocations* (Butterworth-Heinemann, 2001).
21 L. Brewer, M. Othon, L. Young, and T. Angeliu, Microscopy and Microanalysis **12,** 85 (2006).
22 F. Cerdeira, C. Buchenauer, F. H. Pollak, and M. Cardona, Physical Review B **5,** 580 (1972).
23 I. De Wolf, Semiconductor Science and Technology **11,** 139 (1996).
24 S. S. Mitra, O. Brafman, W. B. Daniels, and R. K. Crawford, Physical Review **186,** 942 (1969).
25 S. Anand, P. Verma, K. Jain, and S. Abbi, Physica B: Condensed Matter **226,** 331 (1996).
26 P. Colomban and M. Havel, Journal of Raman Spectroscopy **33,** 789 (2002).
27 E. Anastassakis, Journal of applied physics **86,** 249 (1999).

[28] Y. B. Gerbig, S. J. Stranick, and R. F. Cook, Scripta Materialia **63,** 512 (2010).
[29] Y. B. Gerbig, S. J. Stranick, and R. F. Cook, Physical Review B **83,** 205209 (2011).
[30] M. H. Zaldívar, P. Fernández, and J. Piqueras, Semiconductor Science and Technology **13,** 900 (1998).
[31] J. A. García, P. Fernández, A. Remón, J. Piqueras, V. Muñoz, and R. Triboulet, Semiconductor science and technology **16,** 289 (2001).
[32] J. F. Nye, *Physical properties of crystals: their representation by tensors and matrices* (Oxford university press, 1985).

Figure captions

Figure 1. CL spectra recorded from ZnSe indented samples (a) CVD-grown and (b) recrystallized in Se atmosphere. Insets: SEM images and points (colour dots) inside and outside the indentation (0.1 kp) where CL measurements were recorded. The small spike located at 2.2 eV is an artefact from the CCD camera.

Figure 2. CL spectra recorded from recrystallized sample in Ar atmosphere. Inset: SEM image and points (colour dots) inside and outside the indentation where CL measurements were recorded. The small spike located at 2.2 eV is an artefact from the CCD camera.

Figure 3. (a) Map of the PL intensity ratio between the defects band and the 2.7 eV band. The white dashed lines indicate the position of the edges of the indentation. (b) (Inset) PL intensity ratio between 2.1 eV and 2.7 eV bands, following the white vertical line drawn in (a). The tip of the indentation is located at 10 µm. Selected PL spectra (λ_{exc} = 325 nm) recorded at different points outside (1,2) and inside (3,4) the indentation (0.025 kp) are shown.

Figure 4. (a) Sample axis system defined for the ZnSe sample. (b) Kikuchi pattern recorded on the ZnSe sample. (c) Cubic crystal structure orientation respect to the XYZ axis of the sample. (d) Kikuchi pattern of the twined regions. (e) Inverse pole figure (IPF) for the ZnSe crystal sample. The most intense spot (M points) is close to <221> directions for X, Y and Z axis. The spot marked with a '*T*' correspond to the twins (T points).

Figure 5. EBSD measurements on 0.1 kp Vickers indentation. (a) Orientation of the indentation with respect to the X and Y axis of the ZnSe sample. (b) IPF maps (scale bar of 30 µm) for the three axis X, Y, Z where the crystal misorientation induced by the indentation is visible. Below the IPF maps, the corresponding IP figures are shown. (c) Colour code for the orientation of the IPF maps.

Figure 6. (a) Typical Raman spectrum of the non-indented ZnSe sample, measured with 633-nm laser. The phonon modes identified are indicated. (b) Raman spectrum measured inside the indentation, using the same conditions as in (a).

Figure 7. (a) SEM image of the 0.1 kp indentation. Maps of the (b) intensity (counts), (c) width (cm^{-1}) and (d) position (cm^{-1}) of the TO mode inside and around the indentation, obtained from the fit to Gauss-Lorentzian curves. Raman maps have a scan step of 1 µm.

Figure 8. (a) Optical image recoded using a 10× objective, of indentation preformed with loads of 0.2, 0.1, 0.05 and 0.025 kp (right to left) on the ZnSe surface. (b) Optical image obtained with

the same objective, but with two crossed lineal polarizers, with the sample placed between the polarizers. Birefringent regions are detected around the indentations.

Journal of Applied Physics

AIP Publishing

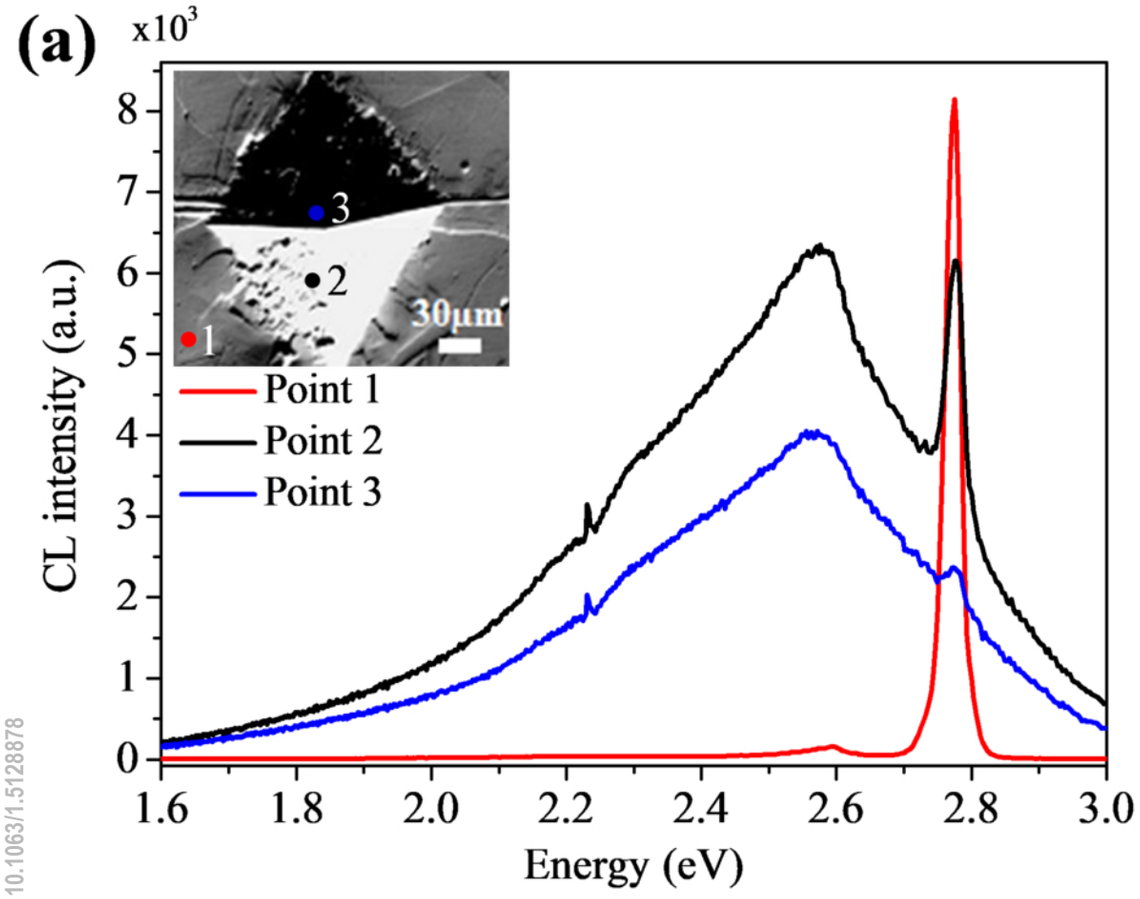

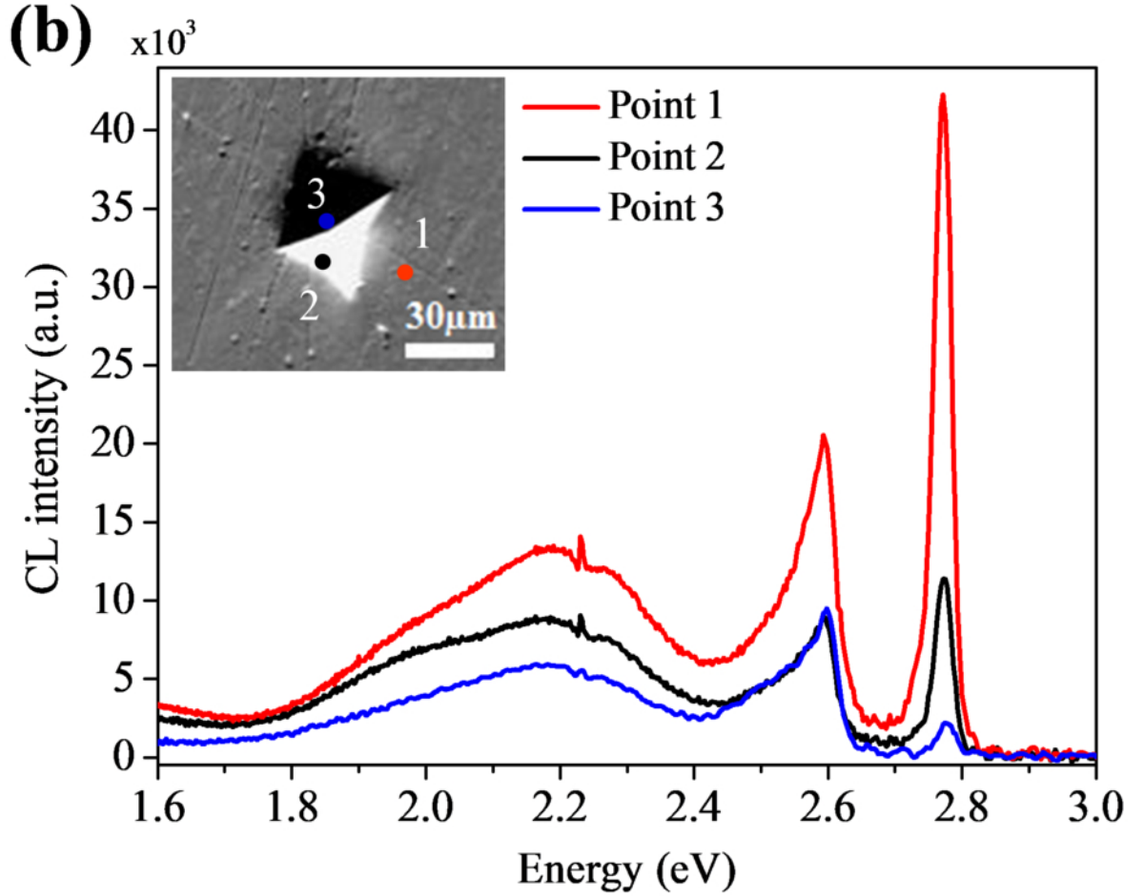

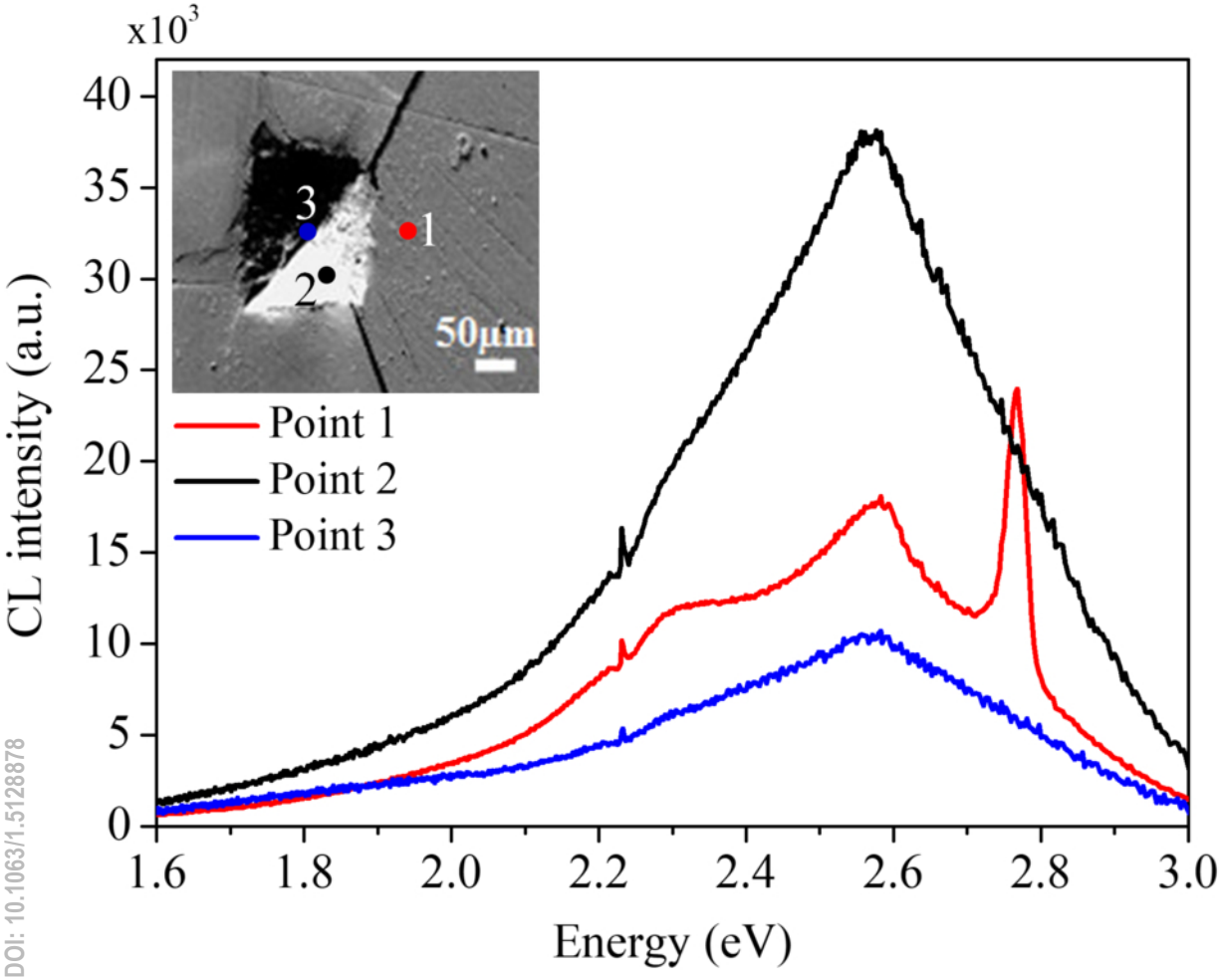

Journal of Applied Physics
AIP Publishing

Journal of Applied Physics

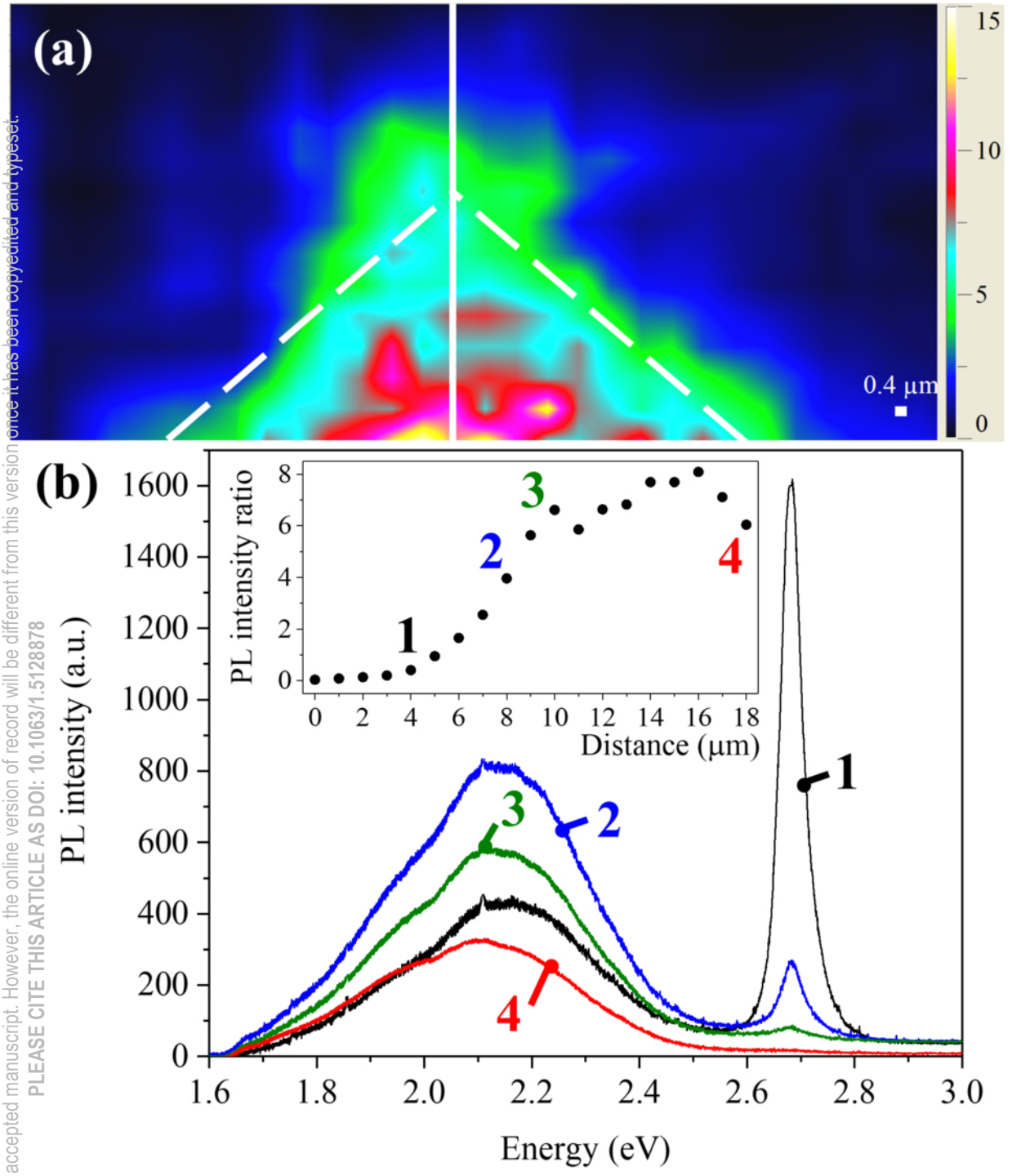

AIP Publishing

Journal of Applied Physics

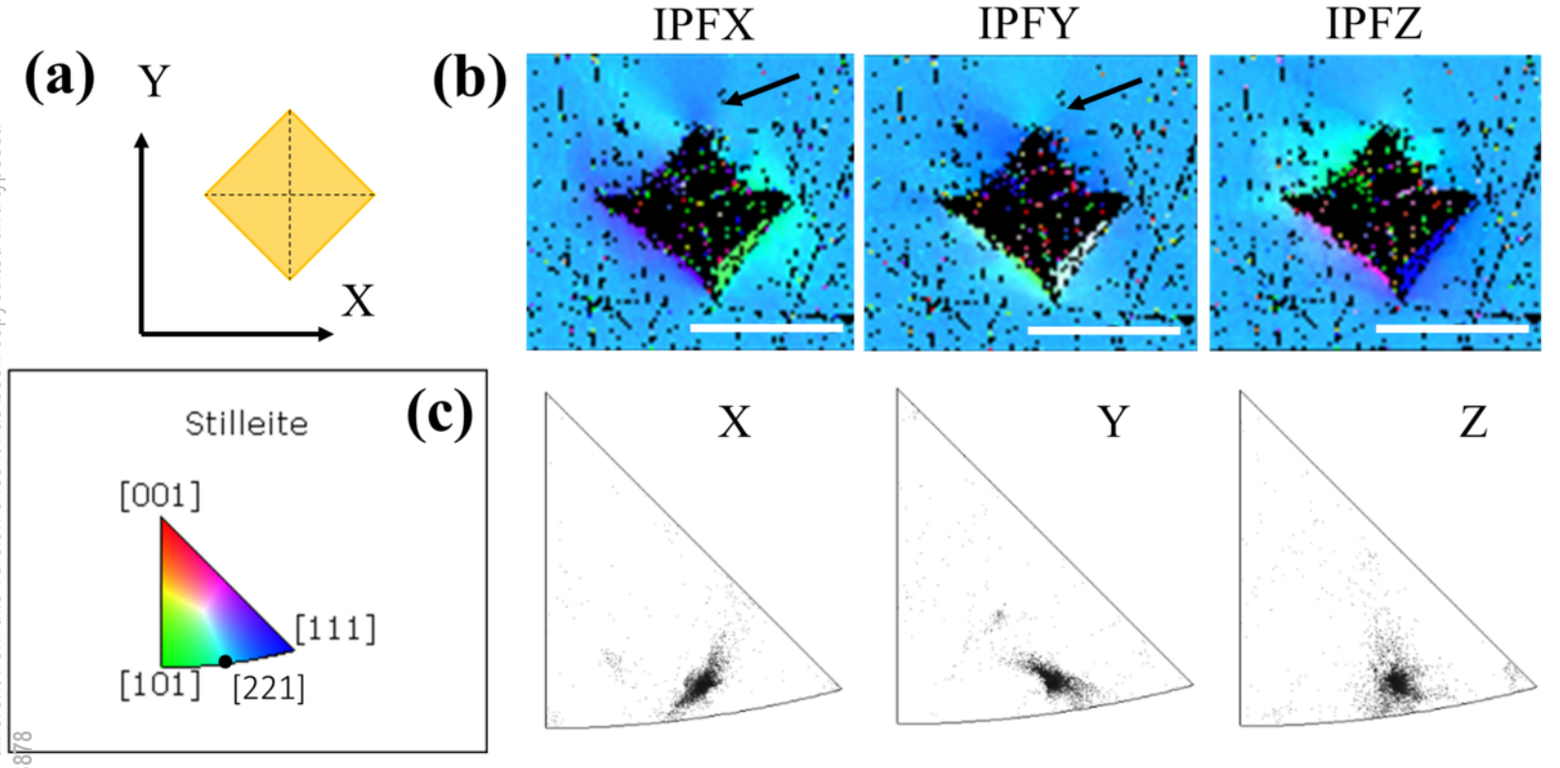

Journal of Applied Physics

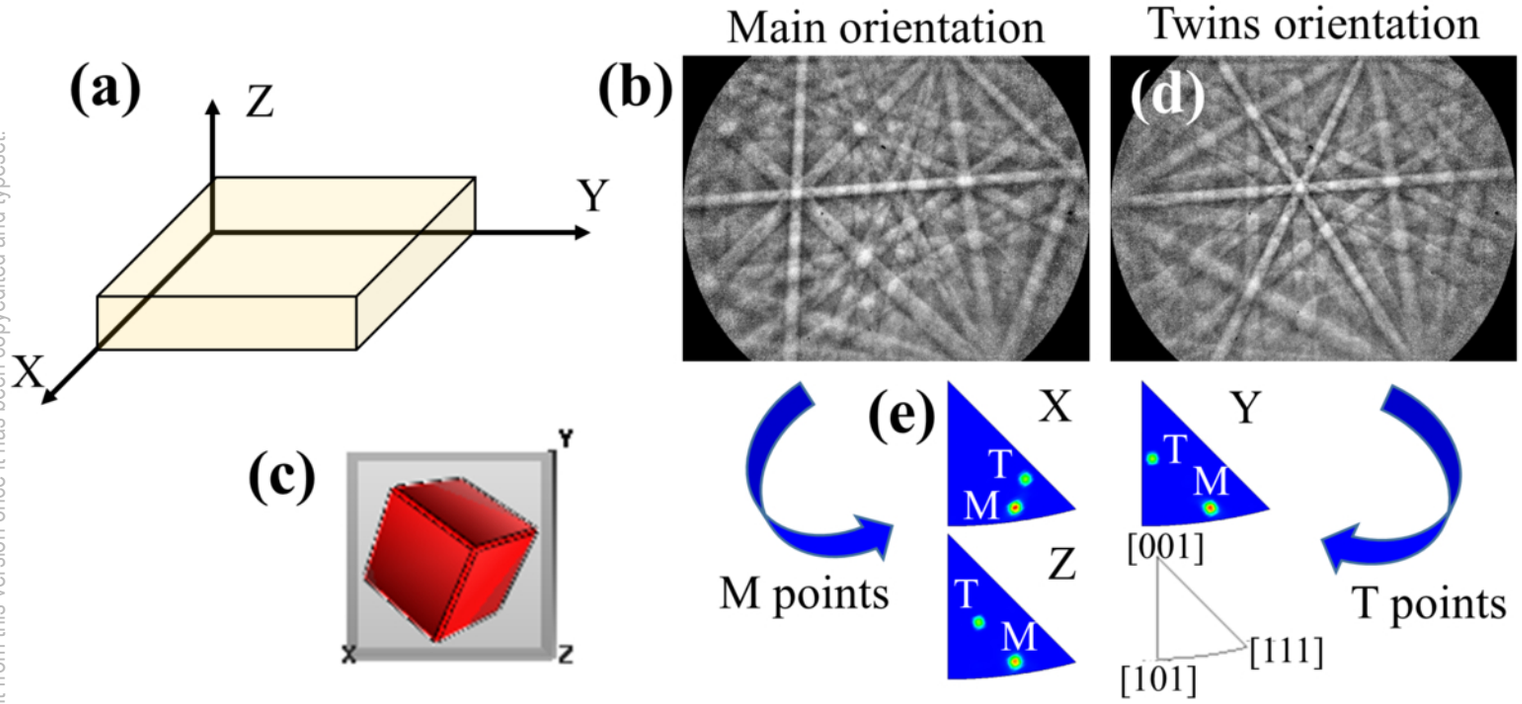

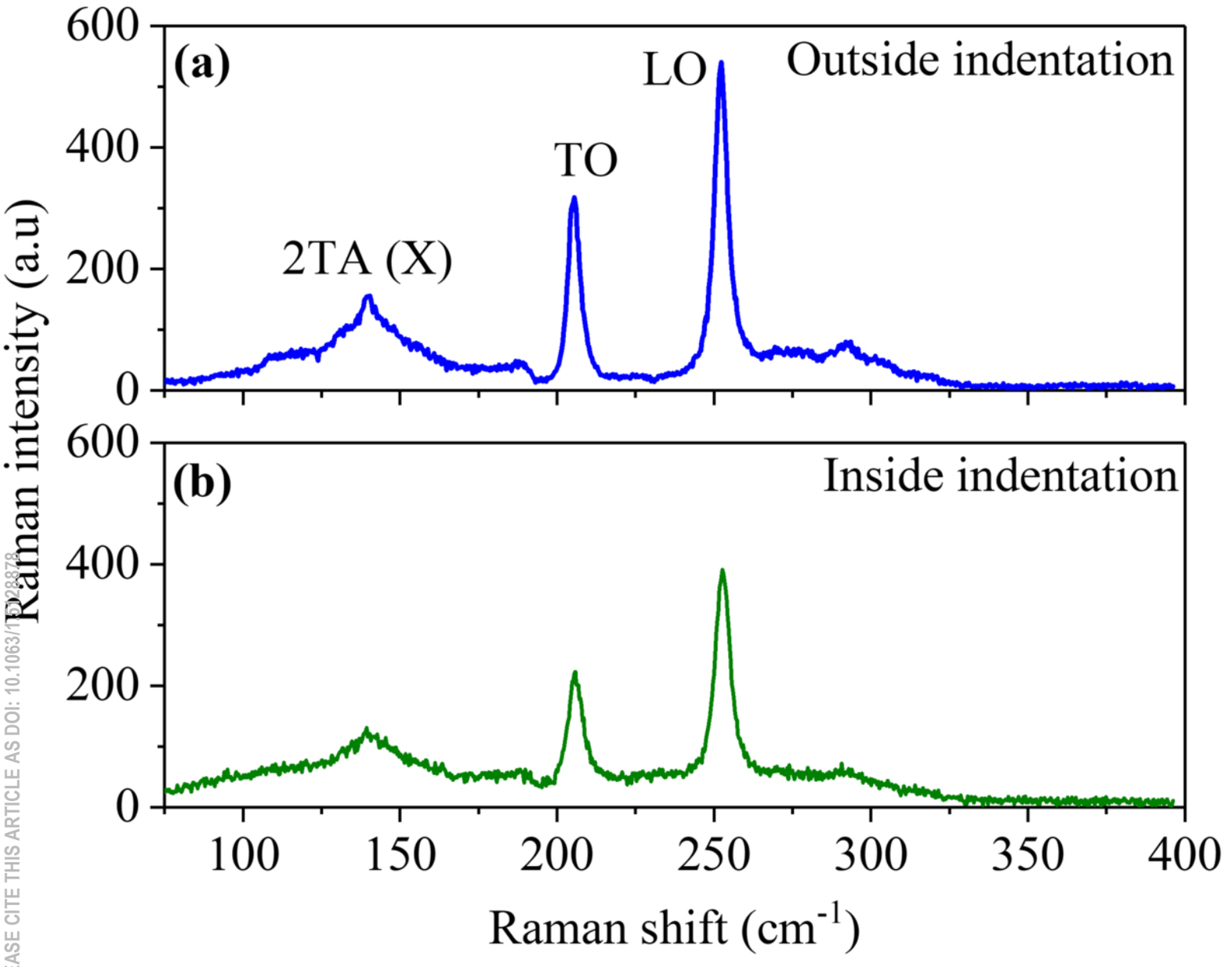

Journal of Applied Physics

AIP Publishing

Journal of Applied Physics

ACCEPTED MANUSCRIPT

PLEASE CITE THIS ARTICLE AS DOI: 10.1063/1.5128878